Supporting Information for "Dead Lithium: Mass Transport Effects on Voltage, Capacity, and Failure of Lithium Metal Anodes"

Kuan-Hung Chen, Kevin N. Wood, Eric Kazyak, William S. LePage, Andrew L. Davis, Adrian J. Sanchez, and Neil P. Dasgupta
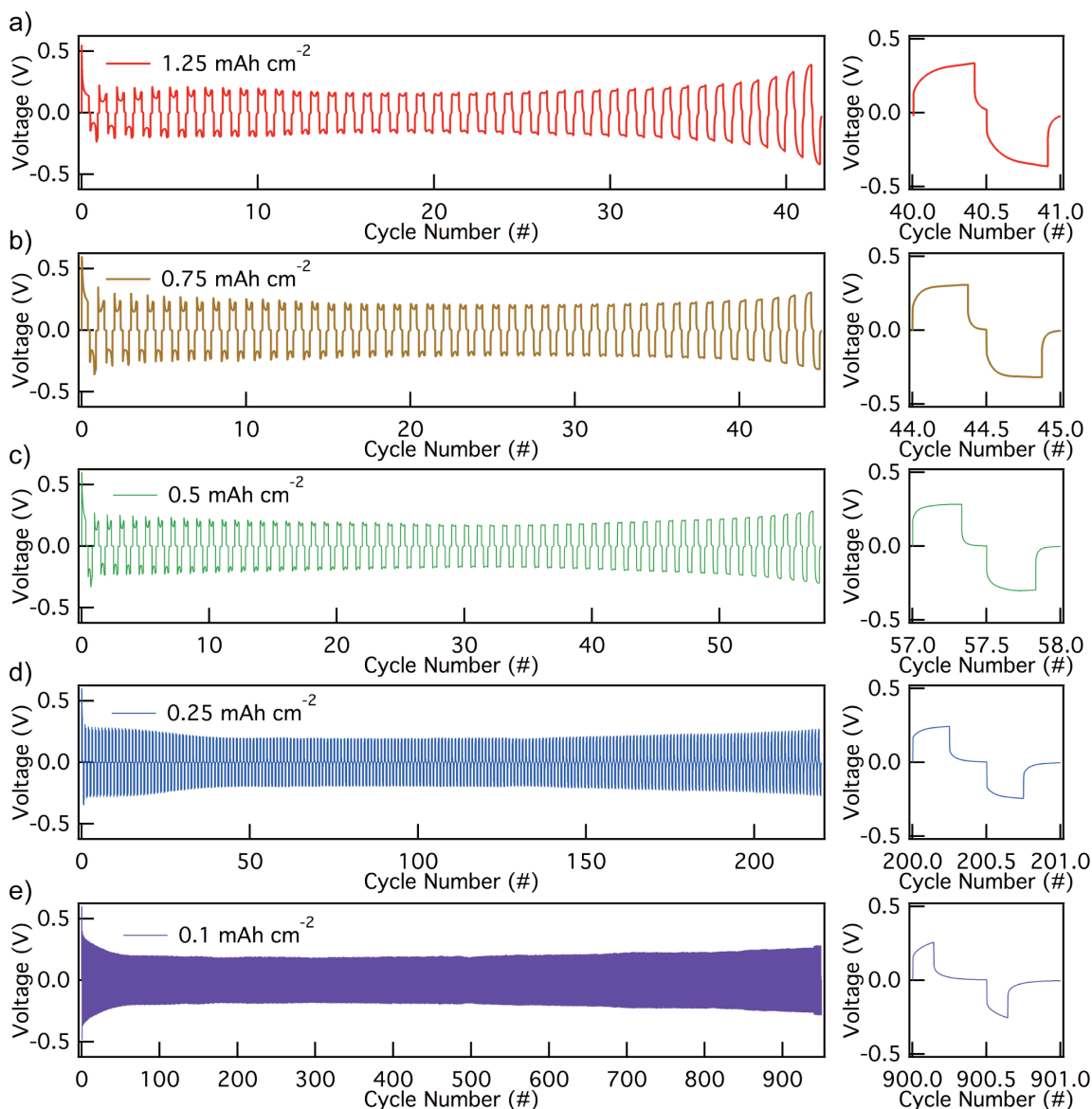
Figure S1. Voltage traces for Li-Li symmetric coin cells cycled at 5mA cm^{-2} at different depth of charge/discharge (a) 1.25, (b) 0.75, (c) 0.5, (d) 0.25, and (e) 0.1 mAh cm^{-2}.
The transition from peaking to arcing behavior is observed over a range of practical depth of charge/discharge. An increase in overpotential is also observed during extended cycling. It is noted that this increase in cell polarization is less abrupt at lower depth of charge/discharge.

1
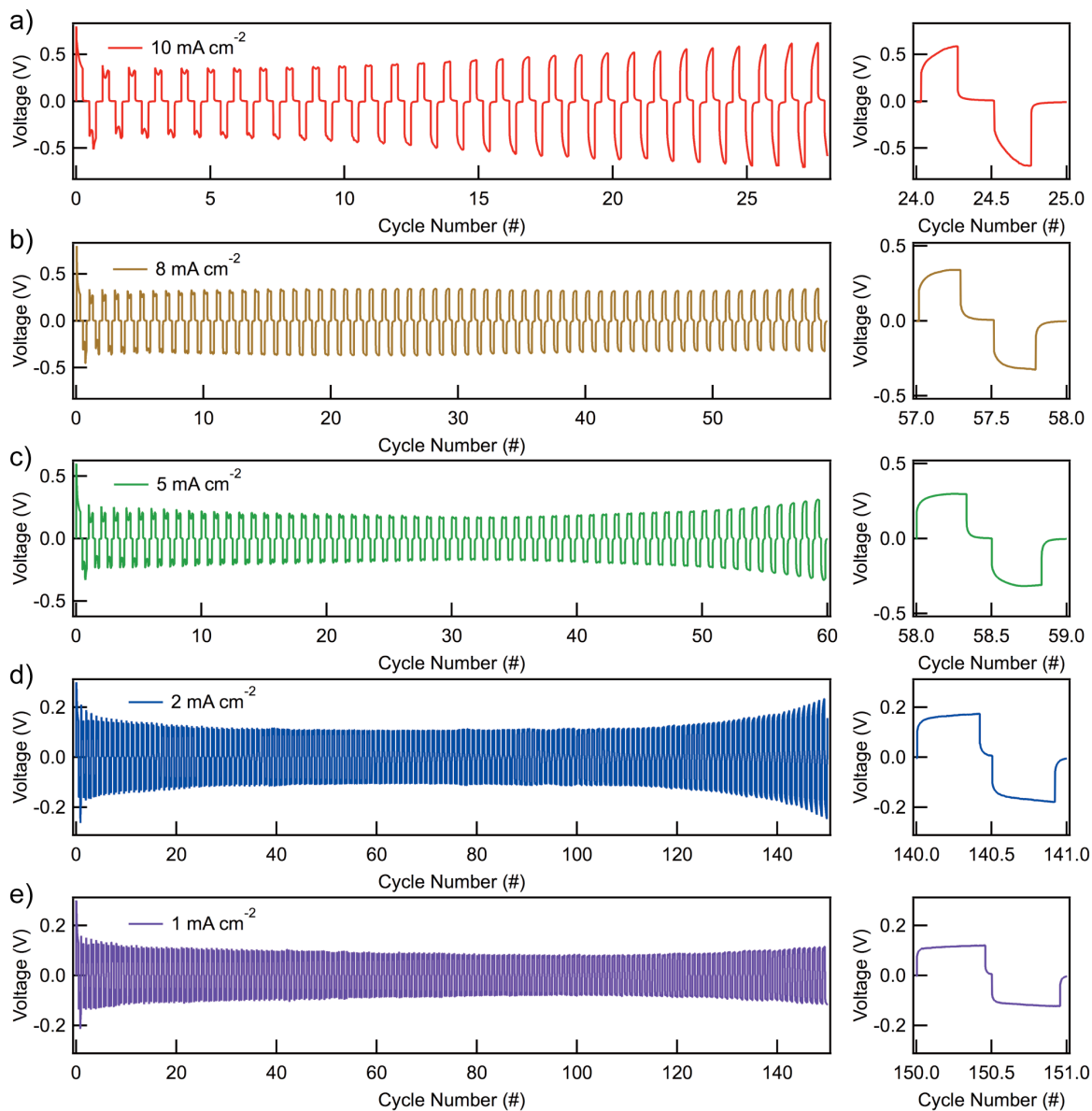
Figure S2. Voltage traces for Li-Li symmetric coin cells cycled at (a) 10, (b) 8, (c) 5, (d) 2, and (e) 1 mA cm^{-2} at fixed depth of charge/discharge of 0.5 mAh cm^{-2}.

The transition from peaking to arcing behavior is again observed over a range of practical current density. An increase in overpotential is observed during the transition period.
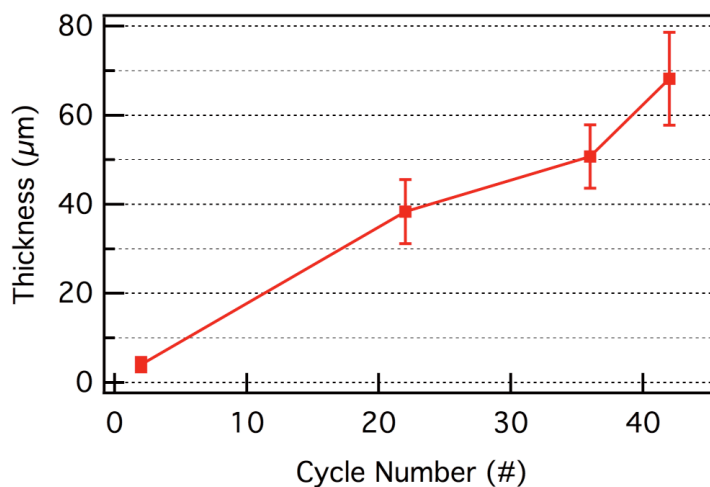
Cycle Number	Average Thickness (μm)	Standard Deviation
2	4.024	1.64
22	38.359	7.21
36	50.751	7.14
42	68.237	10.42

Figure S3. Statistical analysis of the measured dead Li layer thickness from SEM images at cycle 2, 22, 36, and 42.

It is shown that the average thickness of the dead Li layer increases as cycling continues, suggesting that the continuous deposition and dissolution of Li during cycling produce a significant amount of dead Li. 50 measurement points were taken for each respective cycle to calculate the average thickness and the corresponding standard deviation (n=50).
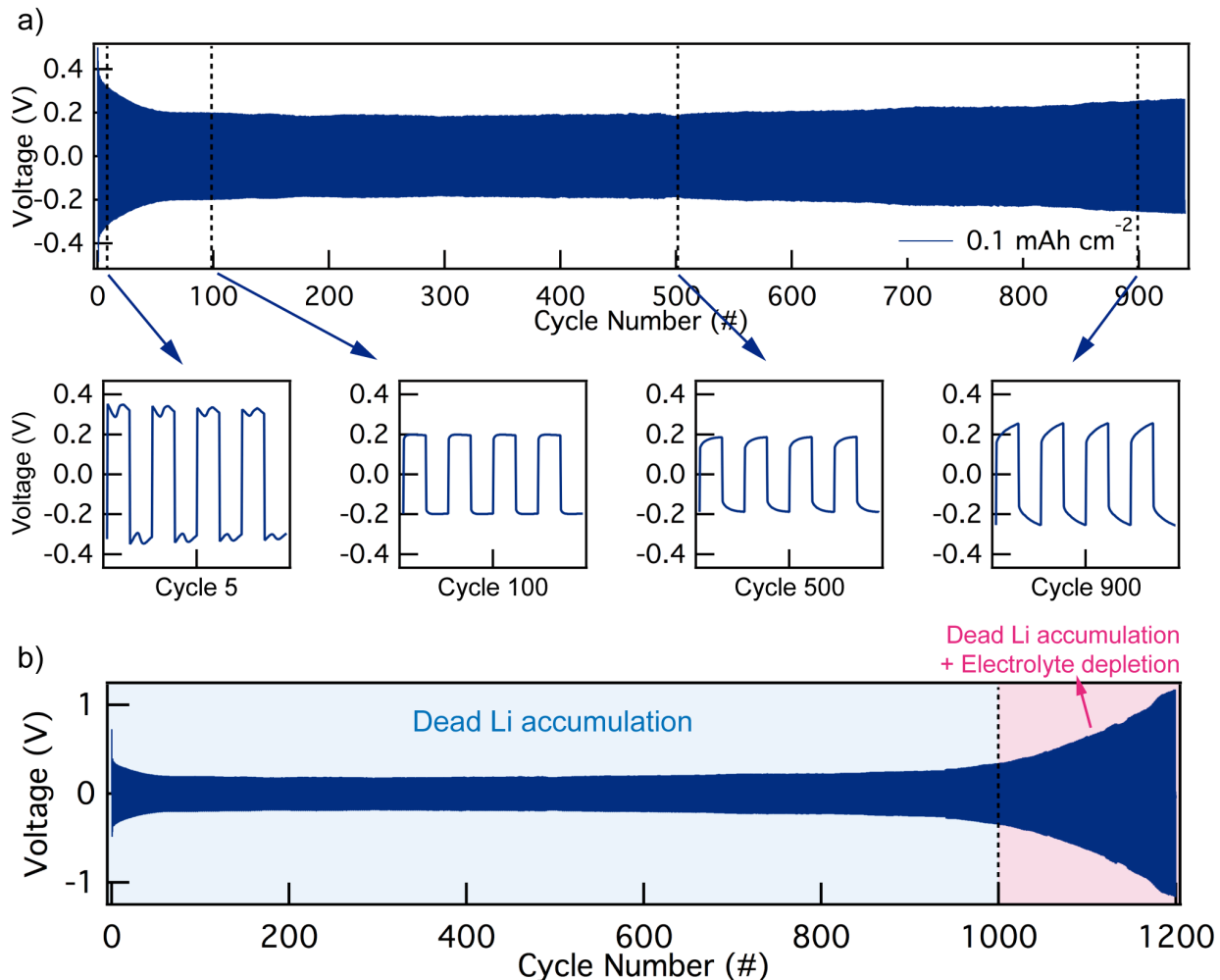
Figure S4. Voltage trace of a Li-Li symmetric cell cycled at 5 mA cm^{-2} at 0.1 mAh cm^{-2}. The transition from peaking to arcing behavior can be seen within the first 100 cycles (cycle 5 and 100). The well-established arcing voltage trace continues to evolve at later cycles (cycle 500, and 900), meaning the characteristic arcs become bigger and reach higher overpotentials toward the end of each half cycle. This evolution can be attributed to the build-up of the dead Li on Li metal surfaces. However, at significant later cycles (> cycle 1000), both degradation of the electrolyte and continued accumulation of dead Li likely contribute to the continued increase in overpotentials.

4
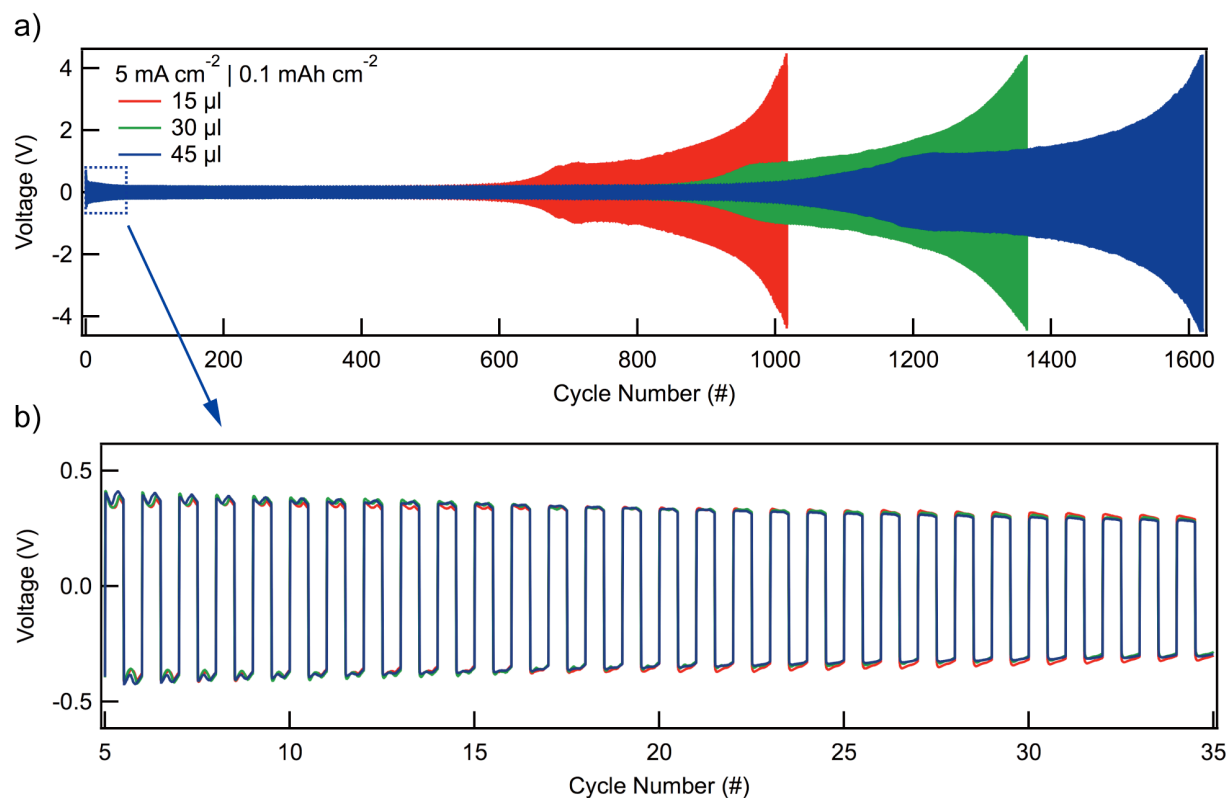
Figure S5. (a) Voltage profiles for three Li-Li symmetric coin cells assembled with different amount of electrolyte and cycled until failure. (b) High-resolution trace of initial cycles to show the transition from peaking to arcing behavior.

While the dramatic increase in the cell polarization near failure is attributed to electrolyte depletion (cell drying-up), the high-resolution voltage traces show that the transition from peaking to arcing takes place at much earlier cycles (cycle 5-35). The onset of the arcing behavior occurs at the same points during cycling, and the corresponding voltage magnitude and shape are also identical for all three cells.
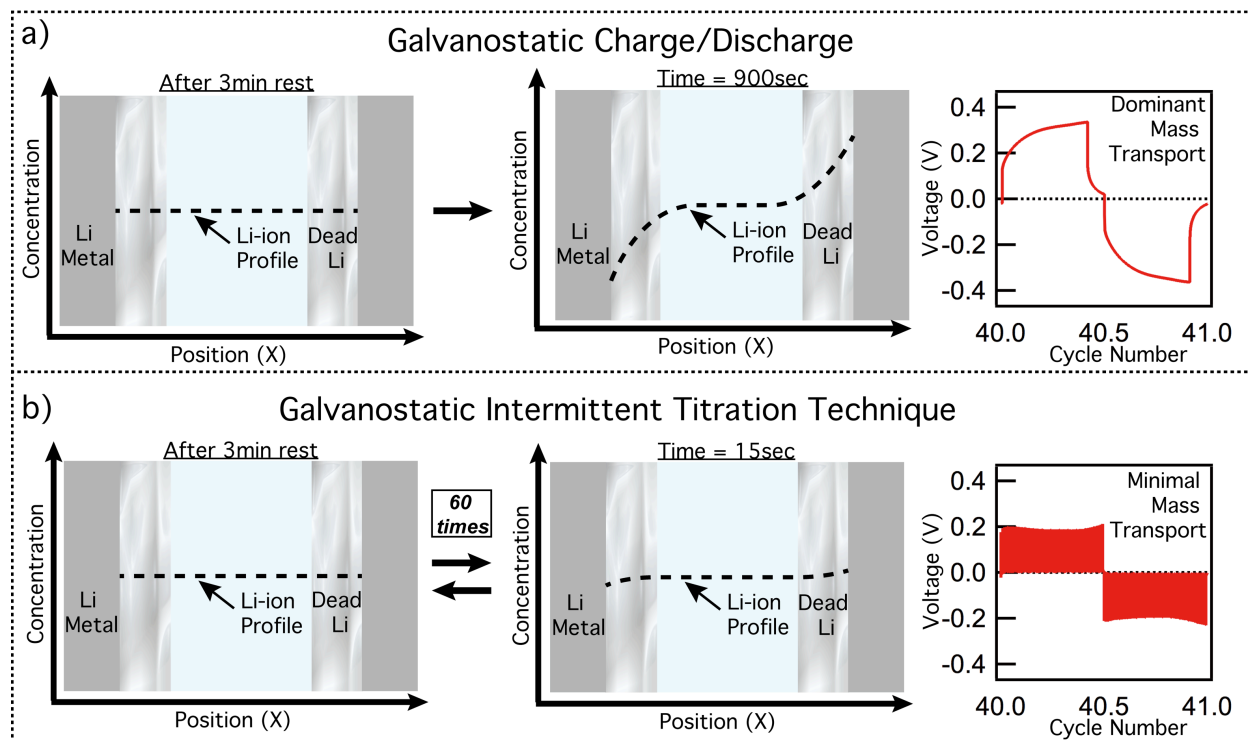
Figure S6. Schematic representation of the difference between (a) galvanostatic cycling and (b) galvanostatic intermittent titration technique (GITT).

During galvanostatic charge/discharge, a greater concentration gradient has to establish in order to maintain a constant Li ion flux across the cell under applied current. GITT enables depositing/dissolving small amounts of Li after a long period of relaxation. Each Li ion can thus be deposited at near static equilibrium conditions (smaller concentration gradient), and experience less effect from the concentration profile of ions at the interphase.
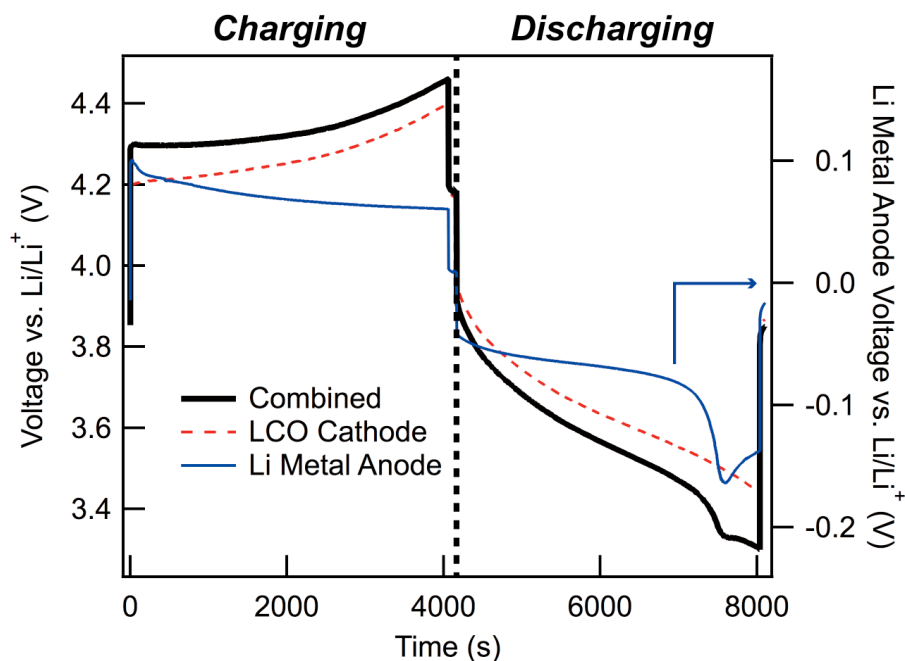
Figure S7. Three-electrode measurement of a Li-LCO full cell shows the cell polarization contributions from both the Li metal anode and LCO cathode during earlier cycles. For visual aid, Li metal anode voltage has been multiplied by -1 such that the total cell polarization (Combined) = LCO Cathode + Li Metal Anode.
The initial peak during the charging cycle is associated with the dendrite nucleation on the Li metal anode surface. During the discharging cycle, a sudden drop in the cell voltage is attributed to the transition of dissolving Li from dendrites to removing Li from the bulk Li metal.
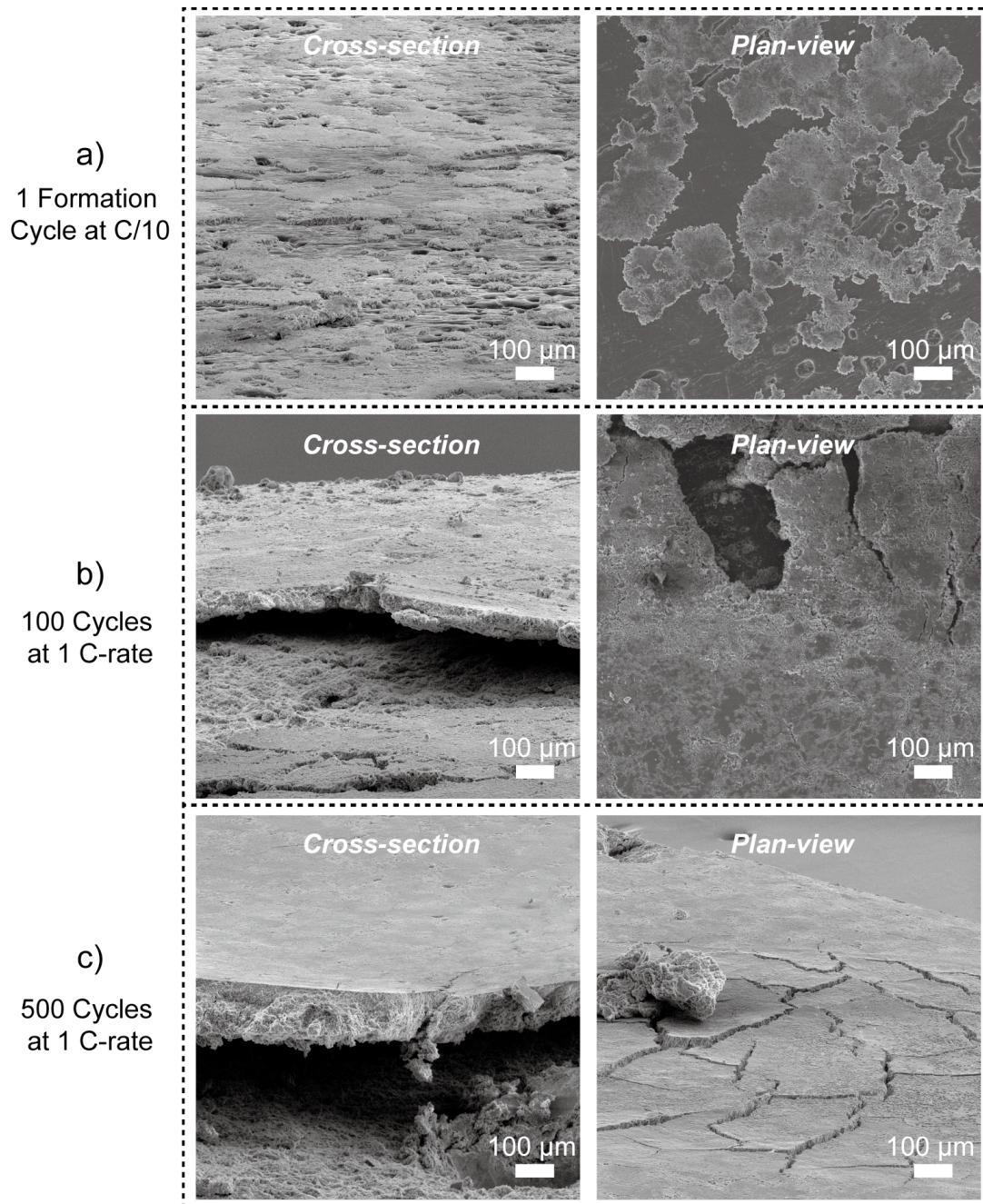
Figure S8. SEM images of Li metal anodes collected from Li-LCO full cells after (a) 1 formation cycle at C/10, (b) 100 cycles at 1C, and (c) 500 cycles at 1C.

A trend nearly identical to that shown for the Li-Li symmetric cell is observed of the Li metal anode in full cells. It is shown that a significant amount of dead Li had built up on the Li metal anode surface after extended cycling, introduced an extremely tortuous pathway for Li ion diffusion across the electrode/electrolyte interphase.
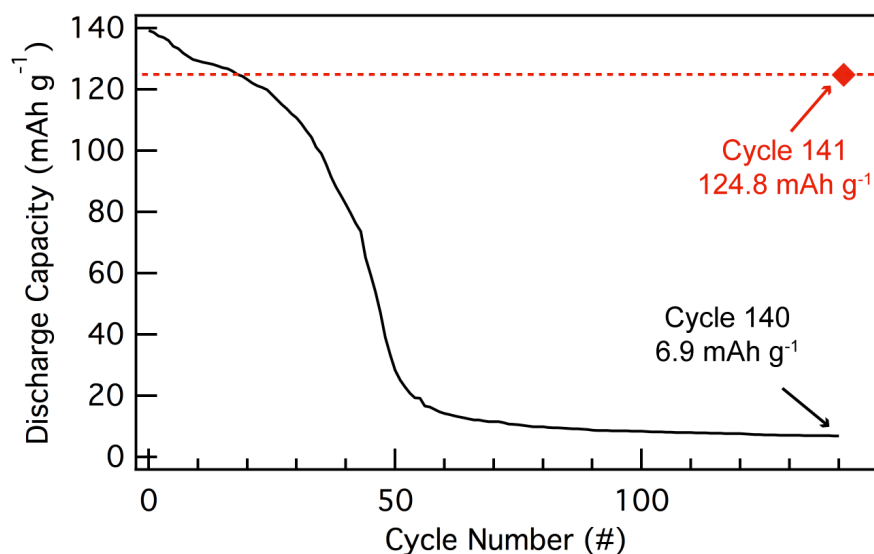
Figure S9. Discharge capacity vs. cycle number was plotted for both the original cell (cycle 1-140) cycled at 1C and the newly assembled cell (cycle 141) cycled at C/10.

The cycled LCO was collected from the original cell after capacity depletion, recombined with a fresh Li metal anode, and fabricated into a new cell. Upon subsequent cycling at C/10, the newly assembled cell exhibited a specific capacity of 124.8 mAh g^{-1}, suggesting that the cathode is relatively stable throughout cycling and is not the main reason for the cell failure at extended cycling.

Cycle Number	Full Cell Capacity (mAh/cm^{-2})	Half Cell Depth of Cycling (mAh cm^{-2})	Cycle Number	Full Cell Capacity (mAh/cm^{-2})	Half Cell Depth of Cycling (mAh cm^{-2})
1	1.86	1.8	51	0.38	0.24
2	1.86	1.8	52	0.34	0.24
3	1.84	1.8	53	0.31	0.24
4	1.84	1.8	54	0.28	0.24
5	1.82	1.8	55	0.26	0.24
6	1.8	1.8	56	0.26	0.24
7	1.78	1.8	57	0.22	0.24
8	1.77	1.8	58	0.22	0.24
9	1.75	1.8	59	0.21	0.24
10	1.74	1.8	60	0.2	0.24
11	1.73	1.68	61	0.19	0.14
12	1.73	1.68	62	0.19	0.14
13	1.72	1.68	63	0.18	0.14
14	1.72	1.68	64	0.17	0.14
15	1.71	1.68	65	0.17	0.14
16	1.7	1.68	66	0.17	0.14
17	1.7	1.68	67	0.16	0.14
18	1.69	1.68	68	0.16	0.14
19	1.67	1.68	69	0.16	0.14
20	1.67	1.68	70	0.16	0.14
21	1.65	1.56	71	0.16	0.14
22	1.63	1.56	72	0.16	0.14
23	1.62	1.56	73	0.15	0.14
24	1.61	1.56	74	0.14	0.14
25	1.61	1.56	75	0.14	0.14
26	1.58	1.56	76	0.14	0.14
27	1.56	1.56	77	0.14	0.14
28	1.54	1.56	78	0.13	0.14
29	1.52	1.56	79	0.13	0.14
30	1.5	1.56	80	0.13	0.14
31	1.48	1.32	81	0.13	0.1
32	1.46	1.32	82	0.13	0.1
33	1.43	1.32	83	0.13	0.1
34	1.4	1.32	84	0.13	0.1
35	1.35	1.32	85	0.13	0.1
36	1.33	1.32	86	0.12	0.1
37	1.28	1.32	87	0.12	0.1
38	1.22	1.32	88	0.12	0.1
39	1.18	1.32	89	0.12	0.1
40	1.14	1.32	90	0.12	0.1
41	1.1	0.96	91	0.12	0.1
42	1.06	0.96	92	0.12	0.1
43	1.02	0.96	93	0.12	0.1
44	0.99	0.96	94	0.12	0.1
45	0.87	0.96	95	0.12	0.1
46	0.8	0.6	96	0.12	0.1
47	0.72	0.6	97	0.12	0.1
48	0.63	0.6	98	0.12	0.1
49	0.52	0.6	99	0.11	0.1
50	0.45	0.6	100	0.11	0.1

Figure S10. Cycle-by-cycle depth of charge/discharge for the Li-Li symmetric cell (Half Cell Depth of Cycling) cycled to mimic the capacity fading in the full cell (Full Cell Capacity).

Depth of charge/discharge for each half cycle is determined by averaging the capacity of the full cell from cycle 1-10, 11-20, 21-30, 31-40, 41-45, 46-50, 51-60, 61-80, and 81-100.
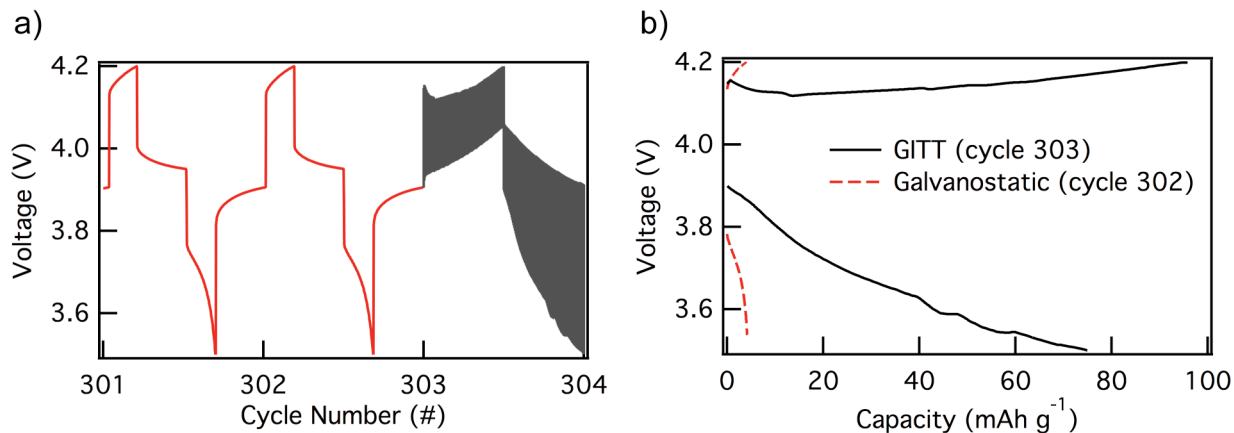
Figure S11. (a) Voltage vs. cycle number and (b) voltage vs. capacity plots of a Li-LCO full cell at cycled at 1 C-rate (1.5 mA cm^{-2}). GITT was carried out at cycle 303 after the cell was galvanostatically cycled for 302 cycles.

The peaking behavior associated with the kinetics of Li metal anode is observed in the GITT voltage trace, verifying that the arcing behavior is due to the mass transport effect. In addition, since GITT can limit the overpotential associated with mass transport, the true cell voltage (V_{oc}) can reach closer to 4.2 V (cut-off voltage). The measured V_{oc} after the GITT charging cycle was 4.06 V, compared to 3.95 V under the previous galvanostatic cycle. As a result, the measured charge capacity during GITT (95.8 mAh g^{-1}) is 22.8 times larger than the previous galvanostatic cycle (4.2 mAh g^{-1}).

Numerical Modeling Details

The numerical model was done in COMSOL and is based on the Nernst-Planck-Poisson equations electrochemistry interface. This interface models the concentration and electric potential profiles within the cell by solving the continuity equation and the Nernst-Planck equation:

$$\frac{\partial c_i}{\partial t} = -\frac{\partial J_i}{\partial x} = \frac{\partial}{\partial x}\left(D_i \frac{\partial c_i}{\partial x} + D_i c_i \frac{z_i F}{RT} \frac{\partial \phi}{\partial x}\right)$$

and Poisson's equation:

$$\frac{\partial^2 \phi}{\partial x^2} = -\frac{F}{\epsilon_0 \epsilon_s} \sum_i z_i c_i$$

where ϵ_0 is the vacuum permittivity and ϵ_s is the dielectric constant of the solvent.[1] For a non-dilute solution system, local variation of diffusion coefficients should be taken into account.[2] In our model, we allow the diffusion coefficient to change with local concentration to more accurately describe the non-dilute electrolyte solution. The results of the COMSOL model were then inserted into the Butler-Volmer equation (equations 2-4 in the main text) to solve for the overpotential at both reducing and oxidizing electrodes.

Figure S12. Schematic showing geometry for numerical model.

A 3-zone geometry was used with different diffusion coefficients in the separator and in the dead Li, as shown in figure S12. The model covered one half cycle (at 5 mA cm^{-2} and 0.5 mAh cm^{-2}) and was run for various thicknesses of dead Li. The boundary conditions used are given in table S1. The parameter values used are given in table S2. The best fit was achived by using diffusion coefficients in the dead Li equal to 1/11 of the diffusion coefficients in the separator. For the diffusion coefficients we used the reported values from previous studies[2,3]. For the effective heterogeneous rate constant we used the k_{fast}^0 value given by our preivious study.[4]

Table S1. Boundary conditions used in numerical model

Quantity	x = 0	x = L
Inward flux of Li^+	-i/F	i/F
Inward flux of PF_6^-	0	0
Electrostatic potential	Floating	Floating

Table S2. Parameter values used in numerical model.

Parameter	Value	Reference
Initial concentration of Li^+	1.0×10^{-3} mol/cm^3	
Initial concentration of PF_6^-	1.0×10^{-3} mol/cm^3	
Current density	5 mA/cm^2	
Time for one half cycle	900 s	
D_0 of Li^+ in separator	2.57×10^{-6} cm^2/s	[2,3]
D_0 of PF_6^- in separator	3.96×10^{-6} cm^2/s	[2,3]
Concentration of metallic Li	7.69×10^{-2} mol/cm^3	
k_{eff}^0	3.5×10^{-6} cm/s	[4]
ϵ_s	16.8	[5–7]
Temperature	25 °C	
Separator thickness	20 μm	

Figure S13 shows the model results for 0 μm, 20 μm and 50 μm of dead Li. During early cycles where the dead Li layer is relatively thin, the contribution of Li-ion diffusion to the cell overpotential is small. During later cycles where the dead Li layer is thicker, there is a much stronger contribution to the cell overpotential because of impeded Li-ion diffusion. The model clearly shows the charactoristic arc during the first part of the half cycle followed by the plateau, demonstrating the same voltage behavior shown in the voltage profiles of the main text.
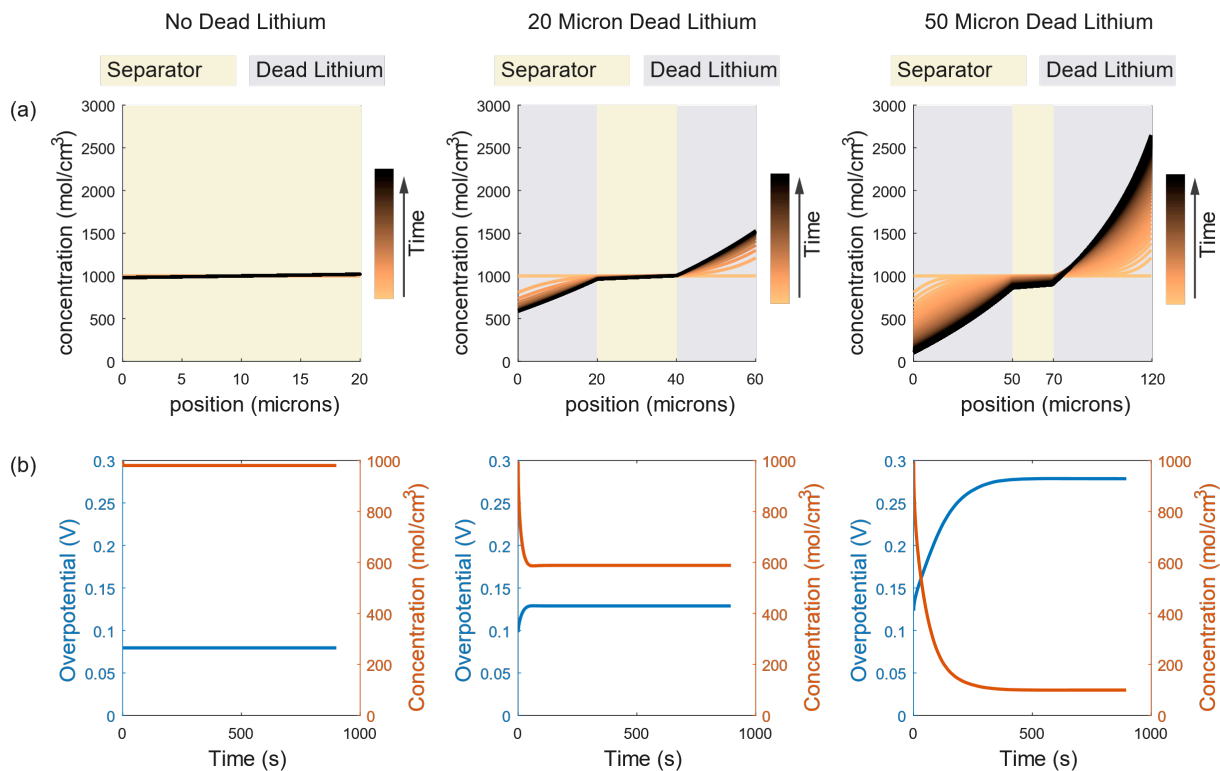
Figure S13. (a) Evolving Li-ion concentration profile for cells with various thicknesses of dead Li. (b) The left axis show the cell overpotential calculated from the Butler-Volmer equation. The right axis shows the interfacial Li-ion concentration at the reducing electrode (x=0).

14

Experimental Details

All air sensitive materials were handled in an Ar-filled glovebox (MBraun), with water and moisture levels below 1 ppm. 1 M $LiPF_6$ (Soulbrain) in 1:1 (volume ratio) ethylene carbonate/ethyl methyl carbonate (EC/EMC) was used as electrolyte in this work, which contained <7 ppm water.

1. Li-Li Coin Cell Testing. Li-Li symmetric cells were assembled with CR2032 coin cell shells, spacers, and wave springs (MTI Corp), each having two Li metal electrodes, one Celgard 2320 separator, and 45 μl of the $LiPF_6$ electrolyte described above. Li foil (Alfa) 0.75mm thick was punched into 1.6 cm^2 discs and were cleaned in pentane with a vortex mixer for 30 seconds prior to assembly into coin cells. A hydraulic crimping press was used to compress these coin cells to 1000 psi. The electrochemical performance of the coin cells was evaluated by galvanostatic charge/discharge on a Landt 2001a battery testing station at room temperature.

2. Li-LCO Coin Cell Testing. The $LiCoO_2$ (LCO) cathode material was provided by CAMP Facility at Argonne National Laboratory. The LCO electrodes with areal mass loading of 14.53 mg cm^{-2} were punched into 1.6 cm^2 discs. Full cells were assembled with one LCO cathode, one Li metal anode, one Celgard 2320 separator, and 45 μl of the $LiPF_6$ electrolyte. The electrochemical performance of the full cells was evaluated by galvanostatic cycling in the voltage range of 3.5–4.2 V. Specific reversible capacity of 1 C-rate was set to 105 mA g^{-1}. The corresponding areal current density value is therefore at 1.5 mA cm^{-2}. One formation cycle was initially conducted at C/10 prior to any subsequent cycling.

3. SEM Characterization. Cycled Li metal electrodes were collected from coin cells for SEM characterization. Cells were first uncrimped using a disassembly die in the same MTI crimping press and electrodes were removed and rinsed with fresh dimethyl carbonate (DMC) for three times before drying in the glovebox. SEM images of the Li electrodes for both the plane-views and cross-sections were obtained with a Tescan MIRA3 GMU FEGSEM.

4. Visualization Cell Testing. Operando optical microscopy was conducted in a custom-built visualization cell[4], allowing simultaneous collection of electrochemical and morphological information. The entire assembly is air-tight with a quartz viewing window and O-ring seal so that it can be removed from the glovebox after assembly and placed under an optical microscope for viewing. Air-tight electrical feedthroughs connect the electrodes with the potentiostat. Visualization cell experiments were carried out using a Biologic VSP potentiostat. The optical microscopy images were taken with a Nikon LV150N microscope at 5x with a plan objective, n.a. 0.10, w.d. 31 mm.

5. Three-electrode Measurements. Three-electrode measurements were experimentally conducted using a hermetically sealed glassware setup. The reference electrode was a scraped, cleaned, and stabilized piece of Li metal foil. The data was collected using the bipotentiostat capabilities of the Biologic VSP system, which can measure the potential of the counter electrode and working electrode vs. reference electrode simultaneously.

Reference

1   J. Newman and K. E. Thomas-Alyea, *Electrochemical Systems*, 2004.

2   L. O. Valøen and J. N. Reimers, *J. Electrochem. Soc.*, 2005, **152**, A882–A891.

3   Y. Saito, W. Morimura, R. Kuratani and S. Nishikawa, *J. Phys. Chem. C*, 2016, **120**, 3619–3624.

4   K. N. Wood, E. Kazyak, A. F. Chadwick, K.-H. Chen, J.-G. Zhang, K. Thornton and N. P. Dasgupta, *ACS Cent. Sci.*, 2016, **2**, 790–801.

5   R. P. Seward and E. C. Vieira, *J. Phys. Chem.*, 1958, **62**, 127–128.

6   Y. Chernyak, *J. Chem. Eng. Data*, 2006, **51**, 416–418.

7   K. K. Karkkainen, A. H. Sihvola and K. I. Nikoskinen, *Ieee Trans. Geosci. Remote Sens.*, 2000, **38**, 1303.